Ⓔ

Coseismic Slip Distribution of the 2010 *M* 7.0 Haiti Earthquake and Resulting Stress Changes on Regional Faults

by Steeve J. Symithe, Eric Calais, Jennifer S. Haase, Andrew M. Freed, and Roby Douilly

Abstract   The 12 January 2010 M_w 7.0 Haiti earthquake ruptured the previously unmapped Léogâne fault, a secondary transpressional structure located close to the Enriquillo fault, the major fault system assumed to be the primary source of seismic hazard for southern Haiti. In the absence of a precise aftershock catalog, previous estimations of coseismic slip had to infer the rupture geometry from geodetic and/or seismological data. Here we use a catalog of precisely relocated aftershocks beginning one month after the event and covering the following 5 months to constrain the rupture geometry, estimate a slip distribution from an inversion of Global Positional Systems (GPS), Interferometric Synthetic Aperture Radar (InSAR) and coastal uplift data, and calculate the resulting changes of Coulomb failure stress on neighboring faults. The relocated aftershocks confirm a north-dipping structure consistent with the Léogâne fault, as inferred from previous slip inversions, but with two subfaults, each corresponding to a major slip patch. The rupture increased Coulomb stresses on the shallow Enriquillo fault parallel to the Léogâne rupture surface and to the west (Miragoâne area) and east (Port-au-Prince). Results show that the cluster of reverse faulting earthquakes observed further to the west, coincident with the offshore Trois Baies fault, are triggered by an increase in Coulomb stress. Other major regional faults did not experience a significant change in stress. The increase of stress on faults such as the Enriquillo are a concern, as this could advance the timing of future events on this fault, still capable of magnitude 7 or greater earthquakes.

Online Material: Figures showing observed and calculated InSAR ranges for tracks 137 and 447.

Introduction

On 12 January 2010, an *M* 7.0 earthquake struck the region of Port–au–Prince, Haiti's capital city (Fig. 1). The event caused more than 200,000 fatalities, left 1.3 million homeless, and caused damage costing close to 100% of the nation's gross domestic product (Bellerive, 2010). The earthquake occurred after about 250 years of relative seismic quiescence in southern Haiti since a series of large events in the eighteenth century (Scherer, 1912; 9 November 1701, 15 September 1751, 21 November 1751, 3 June 1770l; Fig. 1), with magnitude estimates close to or exceeding 7 (Ali *et al.*, 2008; Bakun *et al.*, 2011). The fault segments responsible for these historical events are not precisely known. They may have ruptured the main Enriquillo fault (Fig. 1; Mann *et al.*, 1995) or adjacent, secondary structures, as occurred in the 2010 event (Calais *et al.*, 2010).

Prior to the 2010 earthquake, Global Positioning System (GPS) surface velocities led to the inference that the slip deficit accumulated since 1770 on the Enriquillo fault was sufficient to cause an *M* 7.2 earthquake if entirely released in a single event (Manaker *et al.*, 2008). The 2010 *M* 7.0 earthquake was consistent with this forecast, although it did not rupture the main Enriquillo fault, but a previously unmapped transpressional fault adjacent to it, the Léogâne fault (Calais *et al.*, 2010; Fig. 1). The proximity of the Léogâne rupture to the Enriquillo fault raises concern that the latter may have been pushed closer to failure, as more than 3 million people are currently living within less than 10 km of its surface trace. Quantification of the stress changes on the Enriquillo and other active faults in the region may help determine how seismic hazard in southern Haiti has been altered by the 2010 earthquake (Frankel *et al.*, 2011).

In order to calculate how the 2010 earthquake modified stresses on the Enriquillo and other active faults in Haiti, one must first accurately determine the distribution of coseismic slip for the 2010 rupture. Calais *et al.* (2010) performed a finite-fault slip inversion based on coseismic offsets from GPS and Interferometric Synthetic Aperture Radar (InSAR). They inferred a planar Léogâne rupture with two-thirds
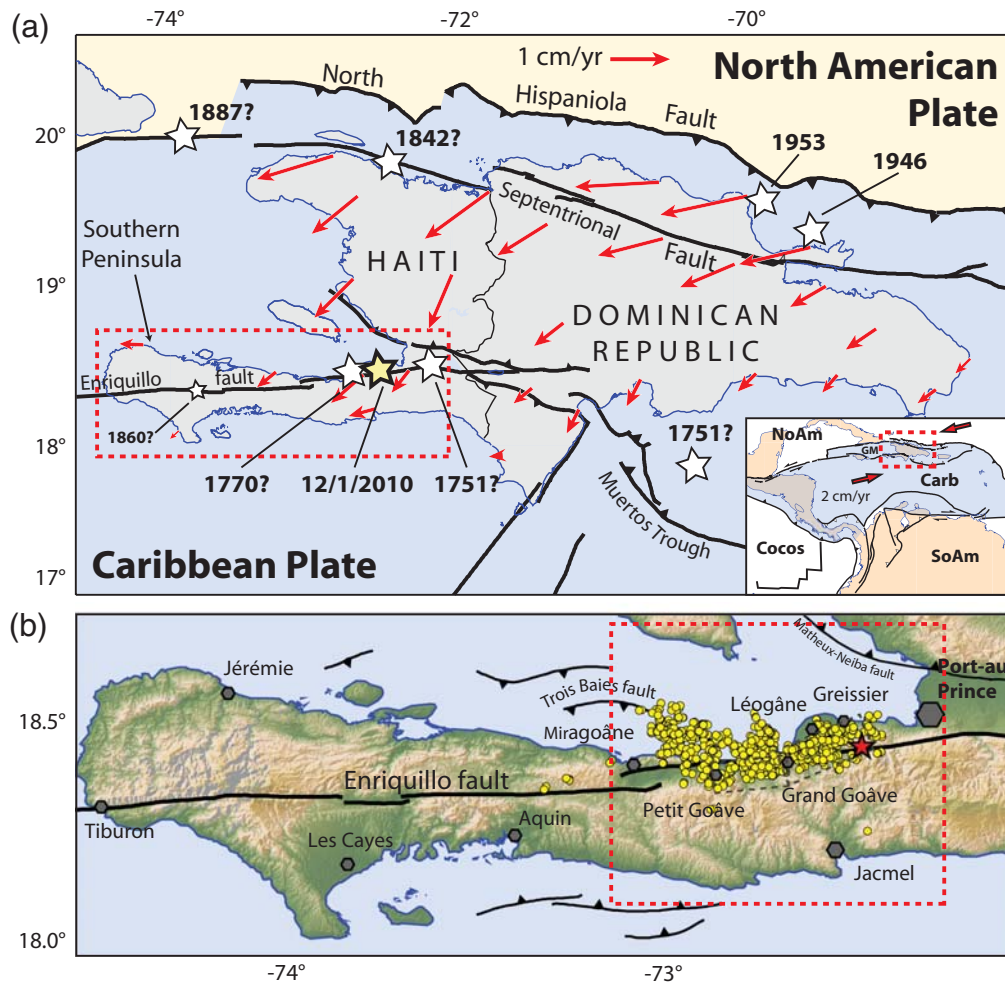
Figure 1. Tectonic setting of the North American–Caribbean plate boundary in Hispaniola. (a) Major active faults (solid black lines, black triangles show reverse faults), large historical earthquakes (stars; Scherer, 1912; Bakun *et al.*, 2011). Red arrows show a selection of interseismic GPS velocities with respect to the Caribbean plate from Calais *et al.* (2010) showing the transpressional nature of the deformation, with significant plate boundary-perpendicular shortening in southern Haiti. Red dashed rectangle shows the area covered on panel (b) below. (b) Enlarged view of the southern peninsula of Haiti. Major urban centers are shown with gray hexagons. Yellow circles show aftershocks as relocated by Douilly *et al.* (2013) for the 10 February 2010–24 June 2010 time interval. The red star shows the location of the 12 January 2010 mainshock from NEIC. The red dashed rectangle shows the area covered on Figure 2a.

left-lateral strike-slip motion and one-third reverse dip slip divided between two slip patches, an eastern one with predominately thrust motion and a western one with predominantly strike slip. Hayes *et al.* (2010), based on a combination of InSAR, coastal uplift, and seismic data, proposed that the rupture initiated on the Enriquillo fault, then transferred to the Léogâne fault, where most of the slip occurred. They also argued for a small amount of slip on a third, south-dipping rupture segment located to the east of the Léogâne fault. De Lépinay *et al.* (2011) used a combination of InSAR and seismic data and an *a priori* rupture geometry derived from an updated source mechanism. They inferred an elongated region of slip with two or three patches of higher slip, with mostly dip slip in the eastern part of the rupture, transitioning to strike slip in its western part, consistent with Calais *et al.* (2010).

Meng *et al.* (2012) used a back projection technique on higher frequency broadband seismic data to resolve two slip patches on two distinct fault segments separated by 20 km. They also performed a fault-slip inversion using lower frequency teleseismic data, which produced two more closely spaced regions of slip. The eastern one corresponds to the Léogâne rupture of Calais *et al.* (2010), whereas the western one is oblique to it and dips to the north-northeast at a much shallower angle. Meng *et al.* (2012) justify their choice of geometry for this western segment on the basis of early aftershock focal mechanisms (Nettles and Hjörleifsdóttir, 2010) and the orientation of the offshore Trois Baies fault (Fig. 1). However, Douilly *et al.* (2013), in a study of precise aftershock relocations, show that many of these large early aftershocks likely occurred to the west of the coseismic rupture. In addition, the Trois Baies fault is known to be a south-dipping structure (Momplaisir, 1986).

At the time of these studies, aftershocks of the 12 January 2010 Haiti earthquake had not been precisely relocated.

Slip-inversion studies therefore had to rely on the imprecise location of the mainshock hypocenter, its source-focal mechanism, and/or geodetic data to provide an initial fault geometry. Recent studies have determined precise aftershock locations and focal mechanisms (Nettles and Hjörleifsdóttir, 2010; De Lépinay et al., 2011; Douilly et al., 2013), enabling an evaluation of the geometry specified in previous rupture models as well as the calculation of a more accurate slip distribution. Here we use the rupture geometry constrained by the aftershocks and use GPS, InSAR, and coastal uplift data to estimate an improved coseismic slip distribution. We then use this updated slip distribution model to calculate coseismic stress changes on regional faults.

Coseismic Slip Distribution

Aftershock Distribution and Rupture Geometry

Shortly after the 2010 Haiti earthquake, Nettles and Hjörleifsdóttir (2010) used teleseismic recordings to calculate refined centroid moment tensor source parameters for $M_w > 4$ aftershocks recorded in the four months following the main event. They found 50 events, most of them located west of the main coseismic rupture. All of the western aftershocks have reverse faulting focal mechanisms with high-angle (30° to 45°) nodal planes oriented N90°E to N120°E. Aftershocks in close vicinity to the mainshock also show reverse-faulting focal mechanisms except for two strike-slip events. The prevalence of reverse-faulting focal mechanisms far to the west of the mainshock led Nettles and Hjörleifsdóttir (2010) to argue for the activation of thrust structures, with strain partitioning between left-lateral slip on the Enriquillo fault and reverse slip on adjacent high-angle faults. In a follow-up study, De Lépinay et al. (2011) used data from a temporary network of ocean-bottom seismometers deployed on either side of the southern peninsula to relocate aftershocks for the 12 February to 7 March 2010 time interval. They found that the aftershocks were divided into two clusters, the first one slightly oblique to the direction of the Enriquillo fault and aligned with the trace of the Léogâne fault, the second one, more diffuse, located mostly offshore and to the west of the Léogâne fault.

Douilly et al. (2013) significantly refined these earlier studies, using all of the local seismological data from temporary deployments recorded from 10 February to 24 June 2010. Using this combined dataset, they developed a 1D velocity model for the region, precisely relocated 1023 aftershocks, and computed first-motion focal mechanisms for 109 events. Their aftershock distribution shows three clusters of aftershocks (Fig. 2). The western one is located offshore in the bay of Grand-Goâve on a plane dipping 45° to the southwest, consistent with the geometry of the Trois Baies reverse fault (Momplaisir, 1986). The central and eastern clusters are located in the Léogâne region. The eastern one delineates a plane dipping 65° to the north, similar in orientation and dip to the Léogâne fault, as inferred from geodetic inversions

(Calais et al., 2010; Hayes et al., 2010), but offset by ∼1.5–3 km to the south (Fig. 2). Reverse faulting in that cluster shows first-motion focal mechanisms with slightly steeper north-dipping nodal planes (60°–75°) than those of Nettles and Hjörleifsdóttir (2010). The trend of the central cluster of Douilly aftershocks is rotated ∼17° counter-clockwise compared to the eastern one, has a steeper dip (70° to the north), and appears to intersect the Enriquillo fault at shallow (∼5 km) depth. There is not sufficient resolution in the Nettles aftershock catalog to determine whether this central cluster is delineating the continuation of the Léogâne fault to the west or represents coseismic slip on a vertical segment of the Enriquillo fault. Uncertainty in the geologically measured dip of that segment of the Enriquillo fault and the scatter of the Douilly shallow-aftershock distribution allow for both hypotheses. However, Douilly et al. (2013) aftershock distribution does not support a rupture scenario with slip on a south-dipping segment of the Enriquillo fault subparallel to the Léogâne rupture or on the fault segment to the east proposed by Hayes et al. (2010). Our models will therefore not consider coseismic slip on these other segments.

We therefore consider two possible coseismic rupture geometries, reflecting the dips and trends observed in the eastern and central aftershock clusters (Fig. 3). Model A is similar to the Léogâne fault geometry described in Calais et al. (2010), but assumes two subfaults with an eastern segment dipping 65° N and trending 248° and a western segment dipping 70° N and trending 264°. Model B uses the same eastern segment as in model A, but assumes that the western segment corresponds to the Enriquillo fault, with a 264° trend and vertical dip with the surface trace offset to the north.

Observational Constraints

We solve for coseismic slip by inverting the GPS and InSAR data previously used by Calais et al. (2010) and the coastal uplift data from Hayes et al. (2010). The InSAR data is from the ALOS/PALSAR system (Japan Aerospace Exploration Agency and Ministry of Economy). It consists of three repeat pairs of radar scenes that provide ground displacement in the radar line-of-sight, about 34.5° from nadir at this location. One interferogram is from a descending orbit (Track 447) determined from data recorded 9 March 2009 and 25 January 2010. The second is from an ascending orbit (Track 138) determined from data recorded from 9 February 2009 and 14 February 2010. The third is from another ascending orbit with data recorded from 28 February 2009 and 16 January 2010 (Track 137). After removing the topographic phase using a digital elevation model, the three sets of data are resampled using a Quad-tree (QT) scheme (Welstead, 1999; Jonsson et al., 2002) to reduce the number of data points while preserving as much information as possible in regions of higher gradients. The three QT datasets used in the inversion consist of 258, 166, and 232 points for ascending track 137, 138, and descending track 447, respectively. The covariance matrix associated with the InSAR data is
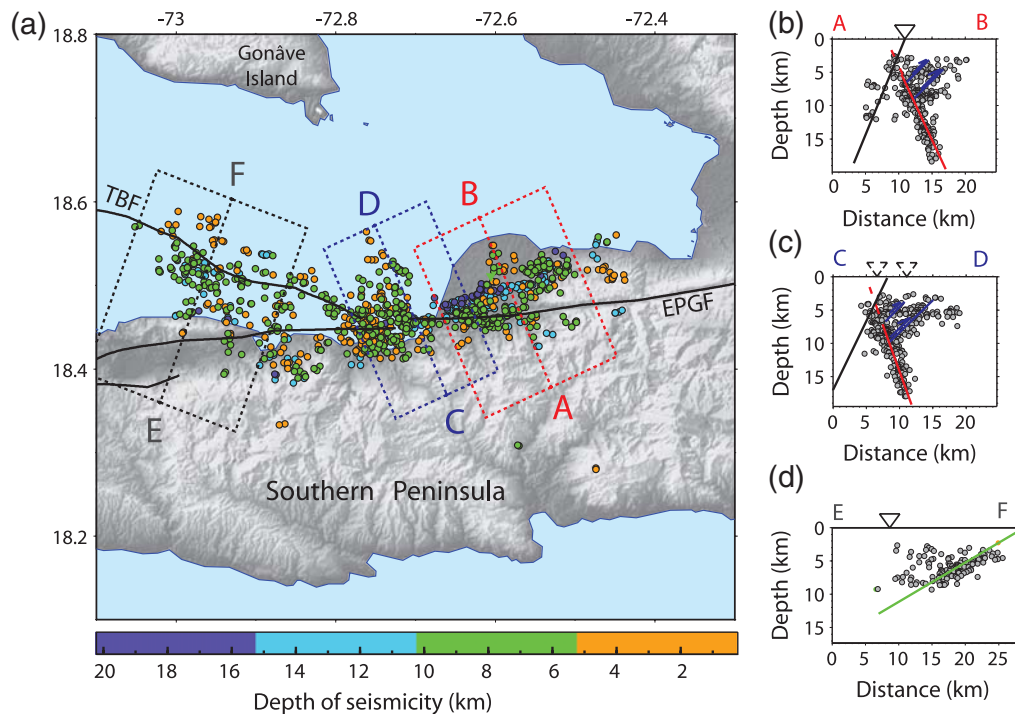
Figure 2. Relocated aftershocks for the 10 February to 24 June 2010 time interval in (a) map view and (b–d) cross section (Douilly *et al.*, 2013). The aftershock distribution shows three clusters; the western one occurs on the Trois Baies reverse fault (TBF), the central and eastern ones occur on the Léogâne fault, which consists of two subfaults dipping 70° and 65° to the north, respectively. Cross sections shows the north-dipping structures delineated by the aftershock distribution associated with the Léogâne rupture (red lines on cross-sections AB and CD) and Trois Baies fault (green line on cross-section EF). Triangle on cross-sections (b) and (d) show the surface trace of the Enriquillo fault. The two black triangles on cross-section (c) show the range of possible locations of the Enriquillo surface trace in this region. The black line is the proposed geometry for the 65° south-dipping Enriquillo Plantain Garden fault (EPGF) at depth. Lines on cross sections represent the fault planes discussed in the text. Black: Enriquillo; red: Léogâne; green: Trois Baies; purple: possible minor antithetic structures or volumetric deformation.
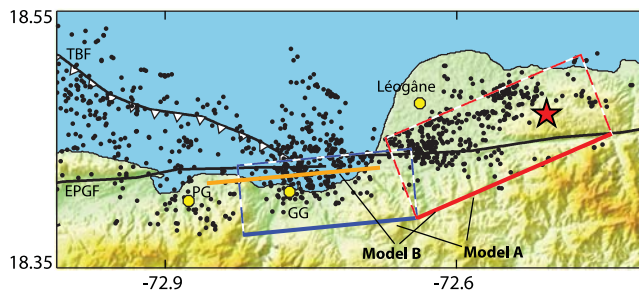

Figure 3. Model rupture geometries tested. Model A considers slip on a northern-dipping eastern segment (L1) of the Léogâne rupture (red) along with slip on a western extension (L2) of the Léogâne rupture (blue). Model B also assumes slip on the eastern segment of the Léogâne rupture (red), but with western slip occurring on a vertical segment of the Enriquillo fault (orange). The red star shows the revised estimate of the mainshock location (Douilly *et al.*, 2013). TBF stands for Trois Baies fault and EPGF stands for Enriquillo Plantain Garden Fault. Yellow circles show cities: PG (Petit Goâve) and GG (Grand Goâve).

derived from variograms and covariograms sampling the noise level in nondeforming parts of the interferograms (Sudhaus and Jonsson, 2009; Calais *et al.*, 2010; their supplementary documents). Standard deviations of range change are on the order of 0.5 mm.

The GPS data consist of position differences between measurements made following the earthquake in January and February of 2010 and measurements made before the event. Pre-event positions were extrapolated to the time of the earthquake using interseismic velocities from the secular strain accumulation model of Calais *et al.* (2010). The GPS data processing method is described in Calais *et al.* (2010, supplementary documents). Uncertainties on coseismic offsets reflect both the uncertainty in individual site positions and in the fitting of a linear model through the position time series for the pre-earthquake time interval. They average 4 ± 2 mm for the horizontal components and 11 ± 4 mm for the vertical component. Site DFRT was excluded from the GPS data because of its location close to the rupture, where the simplified linear geometry used in the inversions is unable to adequately predict surface displacements. Previously, this problem led to large misfits at this station in the Calais *et al.* (2010) slip inversion.

We use vertical coastal uplift data from Hayes *et al.* (2010) based on measurements of uplifted microatolls in the epicentral area. These measurements are consistent with uplift from GPS at Léogâne, where a GPS measurement of 0.5 m is similar to the 0.64 m measured coastal uplift, within

uncertainties. Microatoll uplift uncertainties are estimated to be of the order of 10 cm (Hayes *et al.*, 2010).

Inversion for Coseismic Slip

To estimate the coseismic slip distribution we modeled surface deformation as the result of fault dislocations in an elastic half-space. We discretize the rupture planes using 525 rectangular patches of dimensions 1.25 by 1.3 km. We compute Green's functions that relate slip on each patch to surface displacement at the observation points (Okada, 1992), while assuming a Poisson ratio of 0.25 and a shear modulus 3.3×10^{10} N/m^2. We invert for dip-slip and strike-slip components on each fault patch, applying smoothing via a finite difference approximation of the Laplacian operator (Harris and Segall, 1987; Jonsson *et al.*, 2002) in order to avoid overly rough slip distributions. We also apply positivity constraints by solving with nonnegative least squares in order to avoid rupture with unrealistic slip in opposing directions (Lawson and Hanson, 1974).

The relative weight of the Laplacian smoothness constraint is specified by the smoothing factor, κ, such that

$$\kappa \begin{bmatrix} \nabla^2 & 0 \\ 0 & \nabla^2 \end{bmatrix} \begin{Bmatrix} \mathbf{S}_s \\ \mathbf{S}_d \end{Bmatrix} = \begin{Bmatrix} 0 \\ 0 \end{Bmatrix}, \quad (1)$$

for which ∇ is the Laplacian operator and $\mathbf{S}_s$ and $\mathbf{S}_d$ are the two components of the slip vector. Larger κ values produce spatially smoother slip solutions, but increase the misfit of the data. Although a better fit to observational constraints is often perceived as a more accurate model, such solutions can be biased by the location of instrumentation. Smoother slip solutions tend to mitigate this effect, though the true roughness of coseismic slip is not known.

The trade-off between model roughness (higher model norm) and data misfit as a function of the assumed smoothing parameter is shown in Figure 4 for a range of κ values. Misfit is calculated in terms of χ^2 given by

$$\chi^2 = R^T W_d R, \quad (2)$$

for which W_d is the weight matrix (diagonal here), and $R = d_0 - d_c$ is the residual vector. d_o and d_c are the observed data and the corresponding calculated values. The model norm is given by

$$\text{norm} = (1/\kappa^2)\nabla^2 \mathbf{S}, \quad (3)$$

for which $\mathbf{S}$ is the vector with the slip components estimated on each fault patch.

Figure 5 shows calculated slip distributions and χ^2 misfit for a range of smoothness parameters ($\kappa = 15, 32,$ and 100) using the assumed rupture geometry of model A. Though the slip distributions are similar, we prefer the slip distribution associated with the median $\kappa = 32$, as it represents a balance between accuracy and smoothness. Each slip distribution
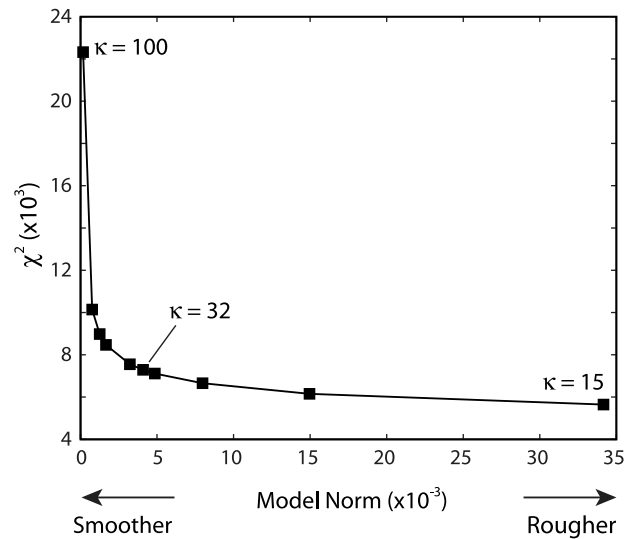

Figure 4.   Model misfit versus Laplacian model norm as a function of the smoothing parameter used in the inversion.

shows two slip patches (one per subfault) centered at 14 km depth, with up to 5 m of slip, similar to the solution of Calais *et al.* (2010). The depth extent of the eastern patch (segment L2) ranges from 3 to 21 km and the western patch ranges from 5 to 18 km, though some surface slip is found on the western segment (segment L1). These slip distributions are generally consistent with the depth of slip found by Calais *et al.* (2010) and with the depth of the seismogenic zone determined from the aftershock distribution (Douilly *et al.*, 2013). The near-surface slip on the western segment in the slip distribution is inconsistent with geological observations that the coseismic rupture did not reach the surface (Hayes *et al.*, 2010). We found that this shallow slip is sensitive to the weight given to GPS site TROU in the inversion, a site located at close distance to the rupture. Removing this site form the inversion also removes this shallow slip, which is not required by the InSAR data alone.

A comparison between the two candidate rupture geometries (Fig. 5) shows that both models produce similar slip distributions. However, model B—in which the western segment (Fig. 5d) is vertical (Enriquillo fault)—shows larger misfits than model A—in which the western patch is north-dipping (Léogâne fault)—in two of the three datasets. We measure the data–model misfit using the weighted root mean square (wrms), given by

$$\text{wrms} = \sqrt{\frac{1}{N} \frac{\sum_{i=1}^{N} \frac{(o_i - c_i)^2}{\sigma_i^2}}{\sum_{i=1}^{N} \frac{1}{\sigma_i^2}}}, \quad (4)$$

for which o_i and c_i are the observed and calculated displacements at site i, σ_i^2, the corresponding observational variance, and N the total number of observations. We find that the wrms decreases by 4% for InSAR data and 3% for GPS data from model A to model B, whereas the wrms for the uplift
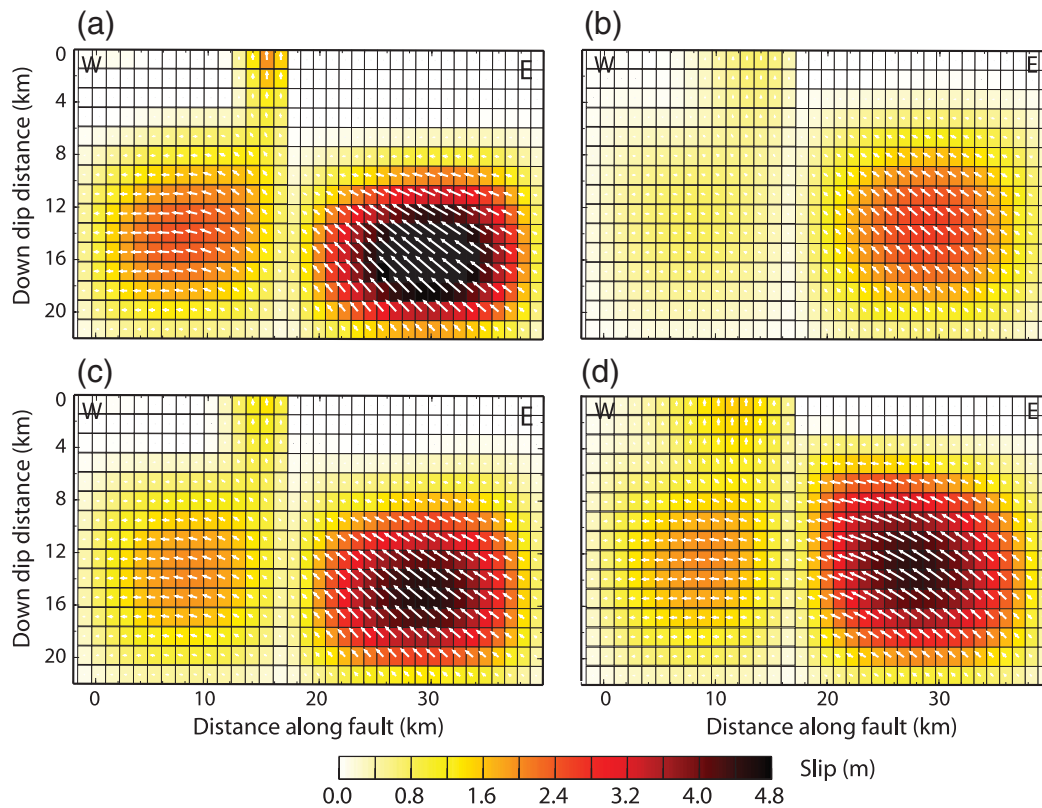
Figure 5. Slip distribution estimated from a joint inversion of InSAR, GPS, and coastal uplift data for four combinations of smoothing parameter κ, and model rupture geometry (Fig. 3). (a) Based on geometry A, $\kappa = 15$, and has a $\chi^2 = 5.8 \times 10^3$. (b) Based on geometry A, $\kappa = 100$, and has a $\chi^2 = 22.2 \times 10^3$. (c) Based on geometry A, $\kappa = 32$, and has a $\chi^2 = 7.2 \times 10^3$. (d) Based on geometry B, $\kappa = 32$, and has a $\chi^2 = 10.6 \times 10^3$.

data increases by 16%. These results, and the likelihood that the Enriquillo fault dips to the south based on observed high topography to the south of its surface trace, leads us to favor the rupture geometry of model A, in which coseismic slip is contained within the Léogâne fault.

In addition to the sensitivity to assumptions for the model geometry and the smoothing parameter, we also consider the relative importance of each of the three observational datasets in the inversion (e.g., Simons *et al.*, 2002; Delouis *et al.*, 2004). The inversion result is indeed weighted towards the largest and best distributed dataset, here the InSAR data, which has 565 sampled points along three satellite tracks. With only 15 coastal surface uplift points and 38 GPS points, these datasets carry much less weight than the InSAR data in the inversion. To this end we investigated a range of models in which we varied the relative weight of each observational dataset by introducing scaling factors to the dataset variance. A higher scaling factor leads to less weight in the inversion and vice versa. We find that increasing the scaling factor on the variance of the InSAR dataset relative to the other two datasets leads to greater misfit (wrms) of the InSAR data, while greatly improving the fit to the GPS data (Fig. 6). The fit to the coastal uplift data is not greatly influenced by changing the scaling factor on the InSAR variances because the number of uplift data points remains too low to strongly

influence the inversion. This can be altered by decreasing the scaling factor in the variance of the uplift data.

Figure 7a–c compares the slip distributions using three different scaling factors, one in which the three scaling factors were all set to 1 (Fig. 7a), one in which the scaling factor on the InSAR data was raised to 10 and GPS and uplift set to 1, and one in which the scaling factor on the InSAR was 10, the coastal uplift dataset to 0.1 and the GPS scaling set to 1. Increasing the scaling on the variance of the InSAR data leads to a broadening of the slip distribution, especially in shallower regions. Decreasing the scaling on the coastal uplift data only modestly influences the slip distribution but notably extends slip in the eastern slip patch (L2) further west to better fit uplift data near Petit Goâve. Figure 7d–f compares surface displacements for each model to the observed horizontal GPS data. As expected, increasing the scaling on the variance of the InSAR data in the inversion leads to a better fit of the GPS data (Fig. 7e). Furthermore, decreasing the scaling on the variance of the coastal uplift data further decreases the GPS misfit (Fig. 7f). Figure 7g–i shows how the scaling factor influences the fit to the coastal uplift data. As with the GPS data, uplift data misfit is minimized for the case in which the scaling factors on the variance of the GPS, InSAR, and coastal datasets are 1, 10, and 0.1, respectively. Figure 8 compares observed and predicted range change as a function
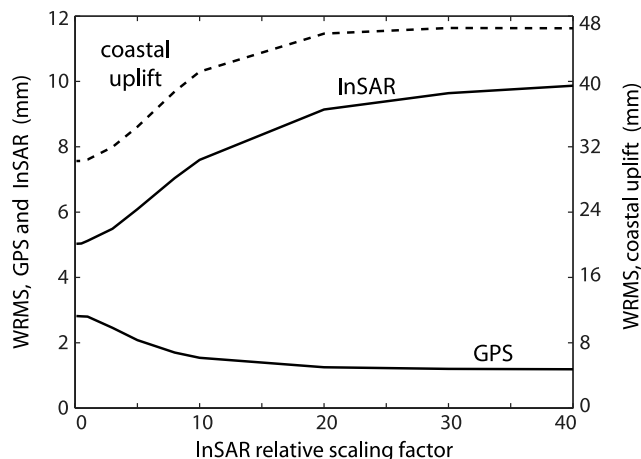
Figure 6. wrms misfit for the three datasets used in the inversion as a function of the scaling factor on the variance of the InSAR data (higher scaling factor translates to lower weighting in the inversion). The lowest InSAR scaling factor considered is 0.05. All models assume model A rupture geometry (Fig. 3) and a smoothing factor of $\kappa = 32$.

of assumed scaling for one of the ascending tracks (track 138). Similar figures can be found in the Ⓔ electronic supplement to this article for the two other InSAR tracks (see Ⓔ Figs. S1 and S2, available in the electronic supplement to this article). As expected, the smallest misfit to the InSAR data occurs for the case in which the scaling factor for the InSAR variance is 1, with the scaling factors of the other datasets set at 1 (Fig. 8b). Decreasing the scaling factor on the uplift data to 0.1 only modestly increases the InSAR data misfit (Fig. 8c) over the case in which uplift and GPS are given equal scaling of 1.

Figure 8 also shows a systematic offset between the observed and modeled interferograms, with the model shifted by 1.5–3 km to the south compared to the data. This suggests that there may be a remaining bias in the aftershock locations used to derive the fault geometry, which were calculated using a 1D seismic velocity structure. However, locations relative to the cluster centroid were calculated with hypoDD (Waldhauser, 2001), which mitigates the effects of 3D structure. Comparable scale studies in the presence of strong crustal velocity contrasts across a fault indicate that hypoDD locations are close to those derived from a 3D velocity model (Douilly et al., 2013, and references therein). In addition, near-source recordings were available for aftershocks that occurred onshore, which also limits the magnitude of location biases. Douilly et al. (2013), however, allow the possibility of a bias up to 1–2 km southward based on systematic travel-time residuals for a few stations in the southern part of the southern peninsula.

Based on these comparisons, we favor the slip model shown in Figure 7c, in which the scaling factors for the variance of the GPS, InSAR, and coastal uplift data are 1, 10, and 0.1, respectively. This model also assumes the fault-plane geometry of model A (Fig. 3) and a smoothing factor $\kappa =$

32 based on the results discussed in the Observational Constraints section. This slip distribution, which we refer to as our preferred solution, is the one used in the Coulomb stress calculations section in this paper. The wrms misfits of this preferred solution are 1.3 mm, 7.8 mm, and 44.0 mm for the GPS, InSAR, and uplift data, respectively.

Figure 9 compares the location of aftershocks on the Léogâne rupture with the slip patches found in the geodetic inversion. Several studies have suggested that aftershocks on the source fault preferentially occur at the edge of large slip patches, due to coseismic stress changes on the rupture plane (Rybicki, 1973; Aki, 1979; Doser and Kanamori, 1986; Hartzell and Heaton, 1986). This is based on the notion that the mainshock of a moderate to large earthquake requires a redistribution of stress within the source fault zone (Mendoza and Hartzell, 1988). Here we find that the central and eastern clusters of aftershocks are generally coincident with the western edges of the two high-slip patches, consistent with these previous studies. The eastern group of aftershocks stops at the end of the eastern segment, which also marks the change in the direction of fault motion. We also observe that both clusters of aftershocks are located in two regions of high gradient in slip and few aftershocks occurred in regions with high slip. This pattern is in agreement with several other aftershock studies (Beroza and Spudich, 1988; Mendoza and Hartzell, 1988; Houston and Engdahl, 1989; Beroza, 1991). The absence of aftershocks above the slip patches, where there is also a large spatial gradient in slip, may be due to the reduced overburden at shallow depth.

Resolution Tests

We carried out resolution tests to investigate the spatial resolution of the slip distribution allowed by the data distribution and uncertainty. These tests consist of forward calculations of surface coseismic displacements caused by given slip distributions on the Léogâne fault, then inversions of the resulting coseismic displacement in an attempt to recover the input slip (e.g., Delouis et al., 2004; Page et al., 2009; Barnhart and Lohman, 2010). The coseismic displacements are 3D GPS displacements, coastal uplifts, and InSAR range changes at the same sites as those in the original data used to determine our preferred slip distribution (see Coseismic Slip Distribution section). In order to simulate the actual noise level in the observations used in the inversions described above, we added 5 mm of random noise to the GPS and uplift data and 10 mm of random noise to the InSAR data. We also used the same smoothing parameter ($\kappa = 32$) as our preferred inversion.

Our first synthetic model tests the ability of the data to resolve shallow and deep slip so that one can rule out the possibility that the lack of shallow slip and the concentration of slip at depth in our best slip distribution model (Fig. 5c) is due to the lack of resolution. We imposed two horizontal strips of 2 m of uniform slip, one located in the top part of the fault (0–6 km), the other in the bottom part of the fault
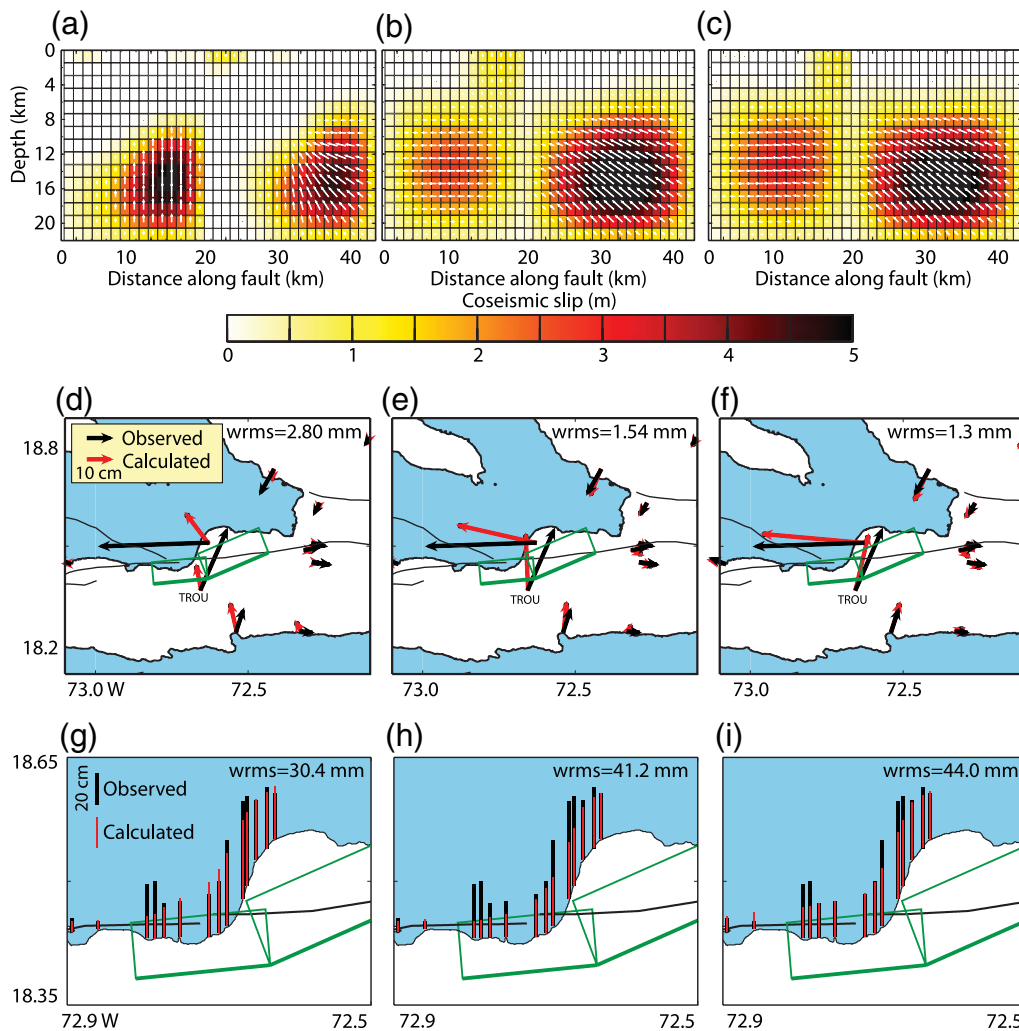
Figure 7. (a–c) Calculated slip distribution as a function of three combinations of scaling factors on the variance of the GPS, InSAR, and coastal uplift datasets (higher scaling factor translates to lower weighting in the inversion and vice versa). (a) The scaling factors are as follows: GPS = 1, InSAR = 1, Uplift = 1. (b) GPS = 1, InSAR = 10, Uplift = 1. (c) GPS = 1, InSAR = 10, Uplift = 0.1. Calculations assume rupture geometry A (Fig. 3) and a smoothing factor $\kappa = 32$. (d–f) Observed and calculated horizontal GPS displacements for each of the corresponding slip distribution models above. The wrms misfit between the observed and calculated GPS displacements is noted in each panel. Surface projection of modeled rupture segments are denoted as green rectangles. (h,i) Observed and calculated coastal uplift displacements for each of the corresponding slip distribution models above. The wrms misfit between the observed and calculated coastal uplift displacements is shown for each panel. Errors on coseismic GPS displacements and coastal uplift were omitted for the sake of clarity. They are 5 mm (horizontal) and 10 mm (vertical) for the GPS, and 10 cm for the coastal-uplift measurements.

(14–20 km; Fig. 10a). Inversion results from the coseismic displacements generated by this input (Fig. 10b) show that we are well able to recover the location of shallow slip on both segments of the fault. However, we recover the deeper slip only in the eastern segment of the fault with some smearing at the edges and underestimated amplitude. We therefore argue that the lack of shallow slip as well as the lack of very deep slip on the eastern slip patch are robust features of our best-fit model.

The second synthetic model tests the ability of the data to resolve two separate slip patches at medium depth, as found in the preferred slip distribution presented above (Fig. 5c). We imposed an input slip distribution with a patch with 2 m of uniform slip in the middle of each of the two

segments of the Léogâne fault (Fig. 10c). The inversion of the coseismic displacements generated by this input slip distribution (Fig. 10d) shows that the two patches are well recovered, with a maximum slip of 1.6 m, although smearing occurs around them.

Finally, we performed a checkerboard test with 11 patches of uniform 2 m slip as input (Fig. 10e). Again, we find that shallow slip is well resolved, with resolution decreasing rapidly with depth for $\kappa = 32$, as shown by the smearing among the intermediate and deepest slip patches. The model was not able to differentiate between these patches and the maximum slip is underestimated at depths below 8 km (Fig. 10f).

These resolution tests show that, given realistic uncertainties, the data configuration has the capability to resolve
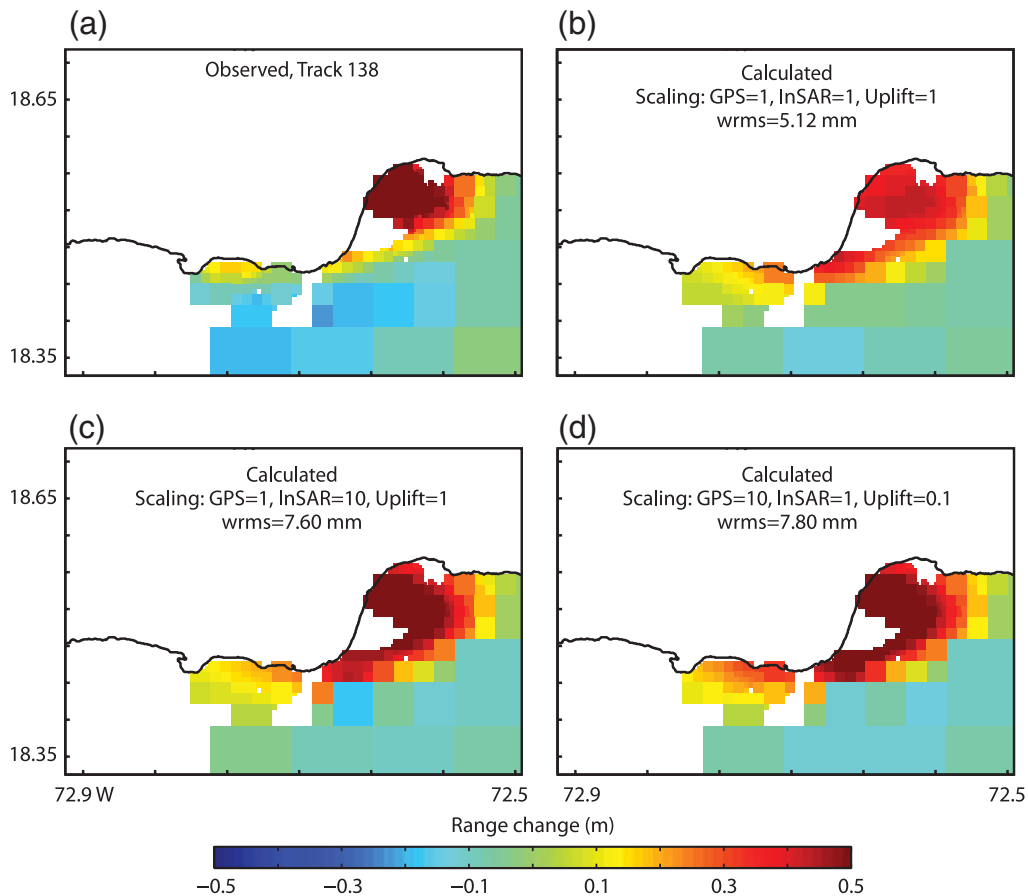
Figure 8. (a) Observed and (b–d) calculated InSAR range change for ascending track 138. wrms misfit between calculated and observed range change is noted in each panel. Calculated range changes are based on the corresponding slip distributions shown in Figure 5a–c. Corresponding figures for InSAR tracks 137 and 447 are shown in Ⓔ supplementary Figures S1 and S2, respectively (available in the electronic supplement to this article).

the lack of shallow slip found in our best-fit model. They also indicate that two major slip patches are likely involved in the coseismic rupture of the 12 January 2010 Haiti earthquake. We cannot resolve whether smaller slip patches might be present below 14 km. In all the models tested, the maximum slip is recovered within 20–40 cm, except in the western patch on Figure 10d. These tests illustrate that the lack of shallow slip in our preferred model is robust. The results make the case that the shallow slip in our best model is resolvable, which leaves an interesting dilemma with regard to the lack of observed surface slip, but possibly suggests a region that should be the focus of further geologic investigations.

Coulomb Stress Changes

Coulomb Stress

Coseismic fault slip causes changes to the surrounding crustal stress field that may influence the state of neighboring faults, possibly causing advances or delays in the timing of future events (Harris and Simpson, 1992; King et al., 1994; King and Cocco, 2001; Freed, 2005; Steacy et al., 2005).

This process is quantified by changes of the Coulomb failure stress (CFS), the combination of the shear stress that drives a neighboring fault to fail and of the normal (or clamping) stress that keeps it from sliding. The change in CFS on a given receiver fault, defined by its strike, dip, and rake, caused by a nearby earthquake is given by

$$\Delta\sigma_\tau = \Delta\tau - \mu \times \Delta\sigma_n, \tag{5}$$

for which $\Delta\tau$ is the change in shear stress, $\Delta\sigma_n$ is the change in normal stress, and μ is the apparent friction coefficient, which accounts for the effect of pore fluid pressure that works to reduce friction. A positive $\Delta\sigma_\tau$ corresponds to a receiver fault being brought closer to failure, whereas a negative change corresponds to failure being delayed (Harris and Simpson, 1992; King et al., 1994). Regions of positive $\Delta\sigma_\tau$ have been shown to coincide with the location of aftershocks, as well as the initiation of several large earthquake sequences (e.g., Reasenberg and Simpson, 1992; King et al., 1994; Stein et al., 1997; Lin and Stein, 2004).

We carried out calculations of $\Delta\sigma_\tau$ in order to investigate whether stress changes associated with the 2010 Haiti
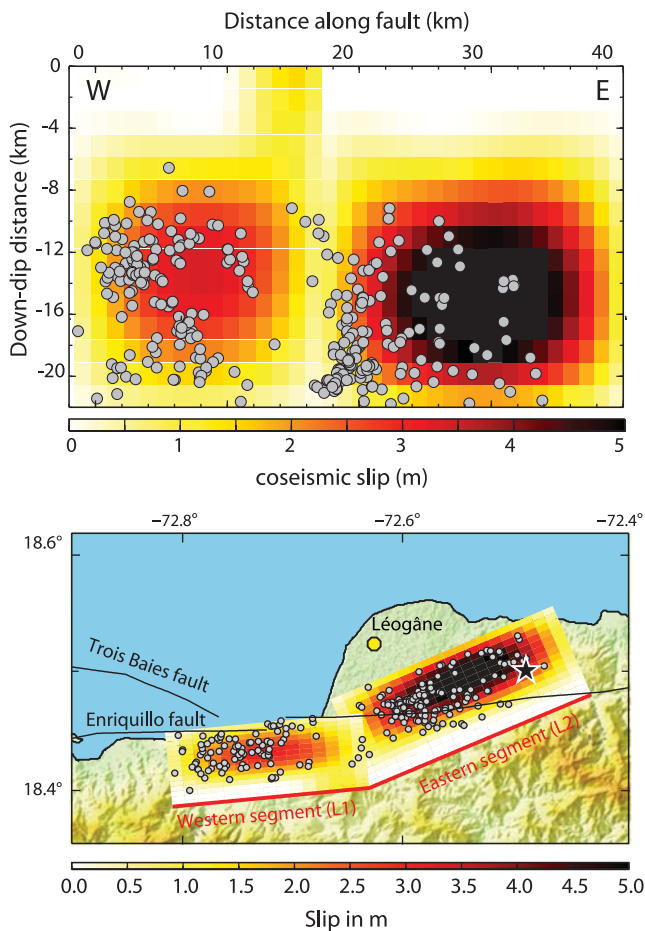
Figure 9. Central and eastern cluster of aftershocks (gray circles) projected onto the best-fit rupture plane with preferred slip distribution model in the background. Only aftershocks located within 4 km of the rupture plane are shown.

earthquake may have had a significant effect on the surrounding faults (Lin *et al.*, 2010). We used the boundary element code Coulomb 3.2 (Toda and Stein, 2002; Lin and Stein, 2004), which uses the formalism of screw dislocations on faults embedded in an isotropic elastic half-space with calculated Green's functions from Okada (1992). The resulting coseismic stresses are projected onto components that are perpendicular and parallel to the rake of each segment of the receiver faults to calculate the corresponding $\Delta\sigma_\tau$. In our calculations, we assumed a range of values of apparent friction from 0.2 to 0.8.

Coulomb Stress Changes on Regional Faults

Calculated Coulomb stress changes for the Enriquillo and all other known major regional faults in southern Haiti are shown in Figure 11, for low and high values of apparent friction. We assume that the Enriquillo fault dips 65° to the south with a rake of 20° based on the orientation of GPS-derived interseismic shortening in southern Haiti (Calais *et al.*, 2010). A dipping Enriquillo fault is also consistent with the higher topography observed to the south of the fault

trace, as reverse motion on a north-dipping Enriquillo fault would result in long-term geologic uplift on the hanging wall side (Prentice *et al.*, 2010). Although it is possible that this dip varies along strike, models that consider shallower dips lead to only moderate differences in calculated coseismic stress changes.

Calculations with low apparent friction ($\mu' = 0.2$, Fig. 11a) show that the Léogâne rupture caused an increase in Coulomb stress (0.1 ± 0.04 MPa) along the shallow portion of the Central and Port-au-Prince segments of the Enriquillo fault, which run subparallel to the rupture. Coulomb stress under these conditions was reduced on the deeper portions of these segments (0.15 ± 0.02 MPa). Calculations that assume high apparent friction ($\mu' = 0.8$, Fig. 11a) led to similar results along the central segment on the deeper portions, but Coulomb stress changes on the shallow Port-au-Prince segment varied from negative to positive (0.1 ± 0.03 MPa). This difference is due to the larger coseismic thrust component in the eastern rupture patch. Though we do not know the apparent friction on the Enriquillo fault, a growing body of evidence suggests that well-developed, primarily strike-slip faults such as the Enriquillo fault are more likely to be characterized by low apparent friction (e.g., Zoback *et al.*, 1987; Parsons *et al.*, 1999). Thus, we tend to favor the low friction model for Coulomb stress calculations on the Enriquillo fault. These stress increases suggest that portions of the Enriquillo fault have been brought closer to rupture, including portions that are closer to populated areas than the 2010 rupture.

Calculations show that Coulomb stress increased to the west of the Léogâne rupture along the Miragoâne segment of the Enriquillo fault (0.2 ± 0.05 MPa), with the increase reaching the base of the seismogenic zone (18 km). The calculated stress increase is greater and deeper here than in any other regional fault segment. This result is not greatly influenced by the assumed apparent friction, though again we would favor the lower friction model. Coulomb stress also increased on the eastern segment of the Enriquillo fault (less than 0.05 MPa) from the surface to the base of the seismogenic zone, but not quite to the magnitude as the Miragoâne segment. For a friction coefficient of 0.8, the increase in Coulomb stress on the eastern segment near Port-au-Prince is negligible.

The Trois Baies fault is an offshore, active, south-dipping, reverse fault mapped by Momplaisir (1986) from seismic reflection data. We have divided that fault into 5 segments (TB1–TB5 in Fig. 11) based on Momplaisir's geological mapping. Each segment is assumed to dip at an angle of 55° based on the approximate dip of aftershocks in this region, and a rake of 70°, as suggested by their focal mechanisms. Figure 11 shows that coseismic slip increased Coulomb stress primarily on segment TB5 (0.08 ± 0.02 MPa), the segment closest to the 2010 rupture, and to a lesser extent segment TB4 (0.02 ± 0.01 MPa). Such values are sufficient to trigger aftershocks (e.g., Reasenberg and Simpson, 1992; King *et al.*, 1994; Hardebeck *et al.*, 1998). These stress
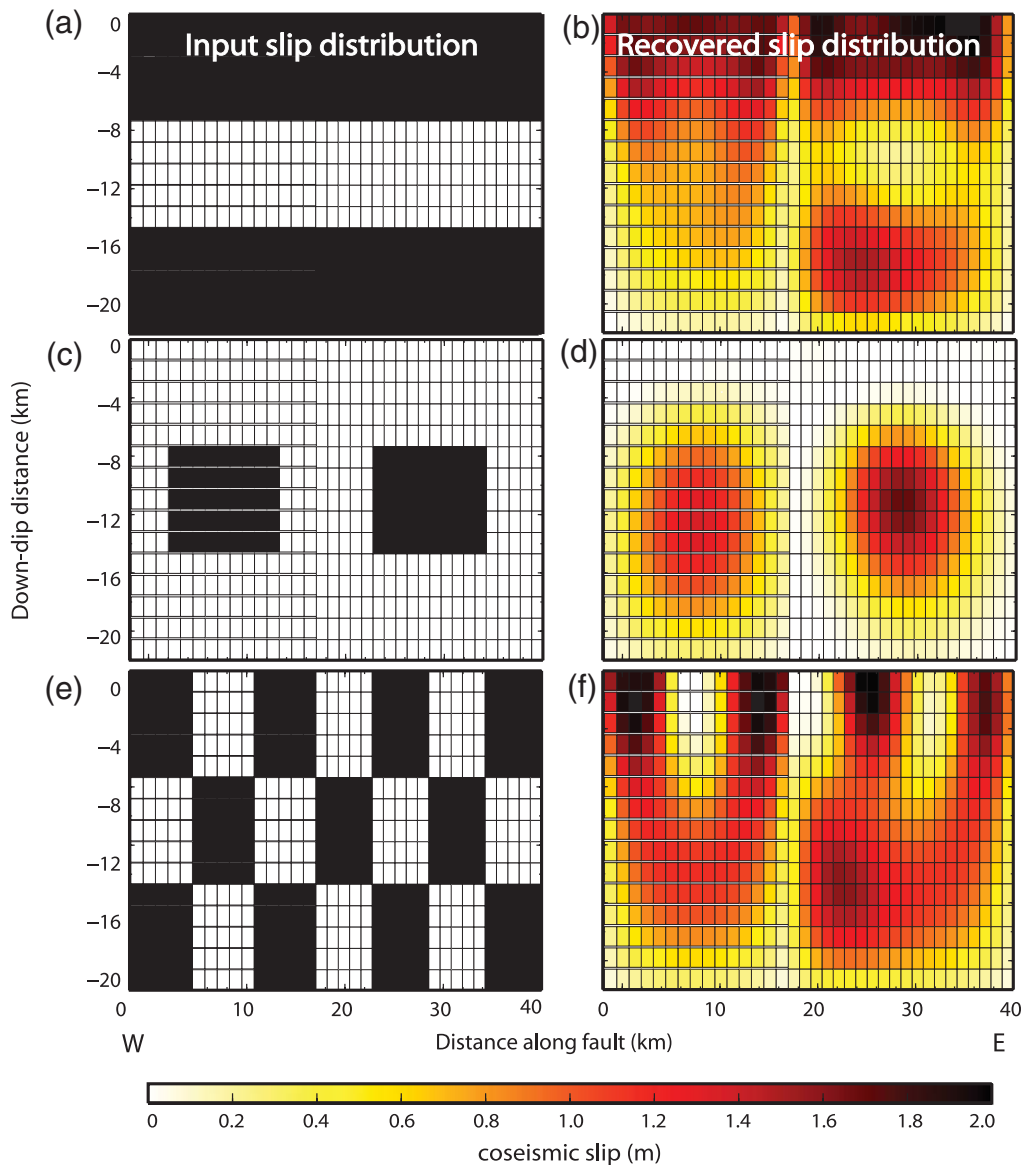
Figure 10.   (a–f) Synthetic slip distribution models and the results. The first column shows the input slip distribution, the second column shows the corresponding output for each model tested. A smoothing of $\kappa = 32$ was used, corresponding to the value used the actual data inversion.

changes are not significantly influenced by the choice of apparent friction. Segments further to the west experienced only a modest change in Coulomb stress, with the sign of the change dependent on the assumed apparent friction. An earthquake on the Trois Baies fault would be hazardous for the cities of Petit-Goâve and Grand-Goâve, especially on a tsunamigenic thrust fault.

To the north, the potentially active Matheux–Neiba thrust fault marks the boundary between the Sierra de Neiba (Dominican Republic), Chaîne des Matheux (Haiti), and the Enriquillo–Plaine du Cul-de-Sac basin at the front of the Haiti fold-and-thrust belt (Pubellier et al., 2000). We consider 5 segments of this fault (NM1–NM5 in Fig. 11) based on the fault orientation. Offshore seismic data between Go-

nâve Island and the coast of Haiti to the northeast indicate recent activity of that fault (Cormier et al., 2010). This fault could take up a portion of the total shortening of up to 2 mm/yr measured by interseismic GPS (Calais et al., 2010). A more recent study (Benford et al., 2012) shows that this fault may be part of a broader deformation zone between the Gonâve and Hispaniola microplates. The precise geometry and sense of slip of the Matheux–Neiba fault are not well constrained. For our Coulomb stress calculations we assumed the fault to be purely reverse, with a dip of 60° and a rake of 90°.

Results show that except for segment NM2, the Neiba–Matheux fault is too far away from the Léogâne rupture to have been significantly influenced (Fig. 11). Whether the NM2 segment has been pushed closer to or further away
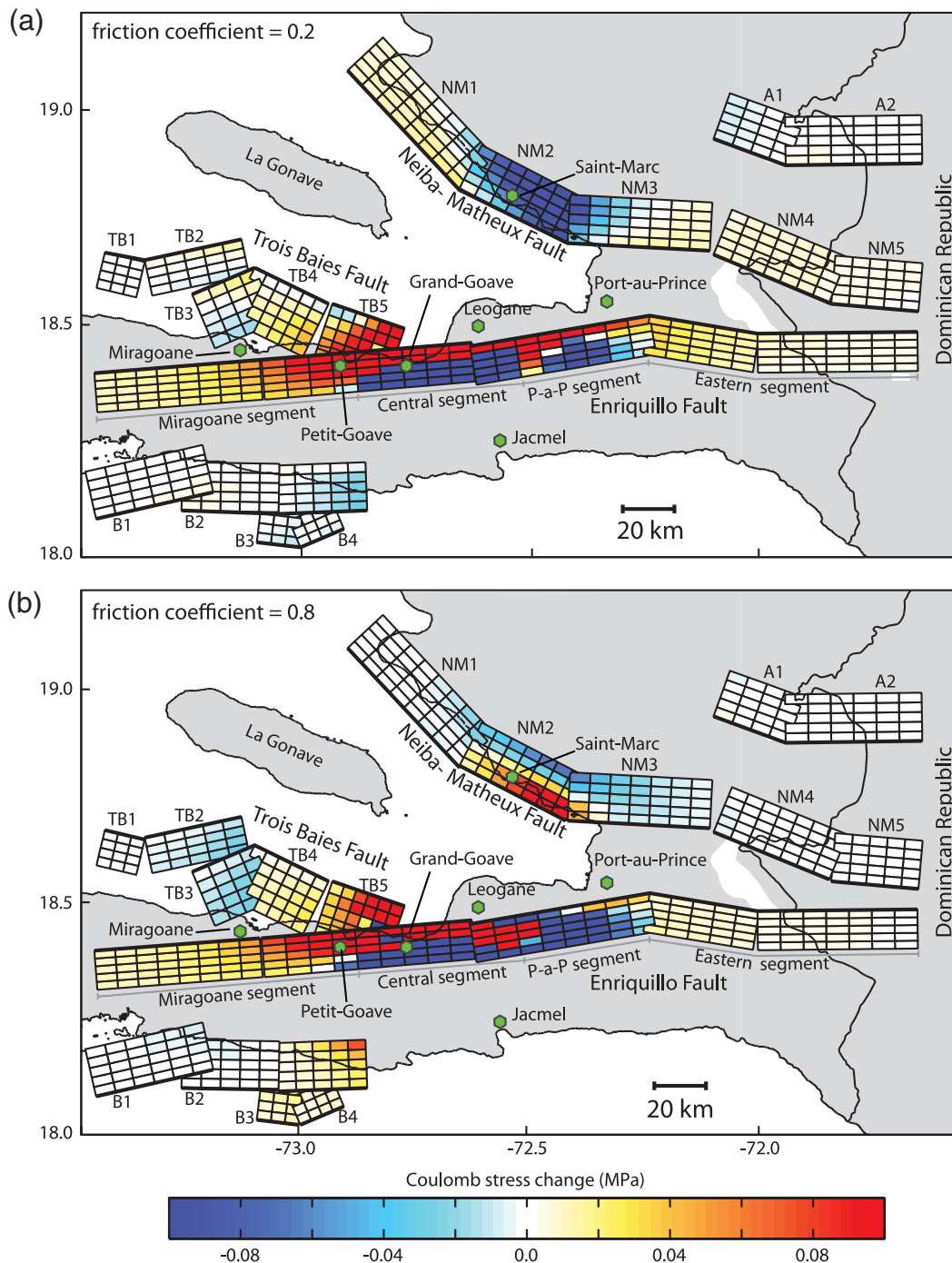
Figure 11.   Calculated coseismic Coulomb stress change on the regional faults of southern Haiti based on coseismic slip associated with our preferred model (Fig. 5c) and two assumptions of apparent friction. The Enrqiullo fault is assumed to dip 65° to the south with a rake of 20°. The Trois Baies fault is assumed to dip 55° to the north with a rake of 70°. All other faults are assumed to dip at 60° and a rake of 90° (pure thrust). Major cities are noted by green circles.

from failure depends on the apparent friction chosen. A low apparent friction leads to a 0.1 ± 0.02 MPa decrease in Coulomb stress (Fig. 11a), whereas a high apparent friction leads to an increase in Coulomb stress (0.1 ± 0.04 MPa) on the shallow portion of this segment. Unlike strike-slip faults, several studies suggest that apparent friction on well-developed thrust faults may be relatively high (e.g., Zoback

et al., 1987; Parsons *et al.*, 1999). Thus, the Coulomb stress increase associated with the high friction case may be more appropriate.

Other regional faults located in the vicinity of the 2010 earthquake include offshore reverse segments to the south of the southern peninsula (segments B1–B4 in Fig. 11) and to the north of the Neiba–Matheux fault (segments A1–A2).

Both were mapped from their bathymetric expression and from oil exploration seismic reflection profiles (Momplaisir, 1986). These reverse faults help accommodate transpressional deformation across the southern peninsula (Benford et al., 2012). We assigned them dips and rakes similar to the Neiba–Matheux fault. Calculations suggest that these faults were located too far from the Léogâne rupture for their stress states to have been significantly influenced.

Testing Coulomb Calculations against Aftershocks

We showed in the Aftershock Distribution and Rupture Geometry section that many aftershocks coincide with the Léogâne coseismic rupture. A number of them, however, occur away from the rupture, possibly lying on nearby faults that were oriented favorably with respect to coseismic stress changes and already close to failure. If the sense of slip of these aftershocks is known, their occurrence can be used to test the coseismic slip model and associated Coulomb stress changes, as ideally aftershocks should preferentially occur in regions of Coulomb stress increase. One should of course expect outliers, as not all aftershocks will follow the dominant stress regime, and aftershocks can be triggered by other aftershocks (Feltzer et al., 2002; Helmstetter et al., 2005).

We initially consider whether aftershocks potentially located on the Enriquillo fault can be explained by coseismic Coulomb stress changes. Figure 12 shows aftershocks located within 2, 4, and 6 km of the Enriquillo fault superimposed on calculated Coulomb stress changes. Aftershocks denoted by yellow circles also lie near the Trois Baies fault, meaning that it is unclear which fault these aftershocks are associated with. In general, we find that aftershocks close to the Enriquillo fault, but not the Trois Baies fault, lie in regions of Coulomb stress increase, while the latter lie in regions of Coulomb stress decrease. Because this Coulomb stress calculation assumes receiver faults with the same sense of slip as the Enriquillo fault, this result is consistent with the yellow circles on Figure 12 being associated with the Trois Baies fault, requiring a different component of stress to determine whether or not their triggering is consistent with the assumed slip model.

To this end we consider the relationship between aftershocks located in the vicinity of the Trois Baies fault (far-western cluster of aftershocks in Fig. 2, cross-section E–F) and coseismic Coulomb stress changes. We therefore calculated Coulomb stress changes in the whole volume using the receiver fault parameters as used in Figure 11 that are appropriate for the easternmost segment of the Trois Baies fault (Fig. 13). We find that virtually all of the aftershocks located near the Trois Baies fault lie in a region of Coulomb stress increase. Based on this result, we can return to Figure 12 and note that if the aftershocks located near the Trois Baies fault in this figure (yellow circles) are not associated with the Enriquillo fault, then the paucity of Enriquillo fault aftershocks at depth is consistent with Coulomb stress decreases.

As one final test of our coseismic slip model, we wished to confirm that aftershocks associated with the Trois Baies fault did not result from coseismic slip on that fault. We ran the inversion described above, but this time allowing slip on the Trois Baies fault in addition to the Léogâne fault. Although the resulting model did place a slight amount of slip on the shallow western portion of Trois Baies fault, it came at the cost of a significantly greater misfit to the data compared to the best-fitting model presented above. In addition, this solution does not significantly alter the slip distribution on the Léogâne fault from that of the best-fitting model. We conclude that it is unlikely that the Trois Baies fault ruptured during the 2010 Haiti earthquake.

Discussion

Implications of the Rupture Geometry

This work and that of Douilly et al. (2013) indicate a possible intersection at depth between the Léogâne rupture and the Enriquillo fault, particularly if the latter is vertical, as is commonly assumed (Mann et al., 1995). We argue here that there is no geometric incompatibility between the two structures.

First, the elevated topography to the south of the Enriquillo fault in the epicentral region (Hashimoto et al., 2011), as well as several direct observations (Prentice et al., 2010), are consistent with the Enriquillo fault dipping to the south. This places the Enriquillo fault to the south of the aftershock cluster that coincides with the western segment (L1) of the Léogâne rupture (Fig. 2, cross-section C–D).

Second, our preferred inversion shows that most of the slip on the Léogâne rupture occurred below 6 km depth, which places the rupture to the north of the 65° dipping south Enriquillo fault at this depth range (Fig. 2, cross-sections A–B and C–D). This is clear for the eastern segment (L2) of the rupture, where the surface trace of the Enriquillo fault is well-determined on land. For the western segment (L1) of the rupture, the surface trace of the Enriquillo fault is not well known and located offshore. It has been proposed that it lies very close to the shoreline (Fig. 2 of McHugh et al, 2011). Assuming a 65° dip, the slip patch below 6 km depth would also fall north of the Enriquillo fault plane.

The available geological information on the Enriquillo fault (surface, trace, and dip), the precisely relocated aftershocks, and the geometry of the coseismic slip regions (depth and dip) are therefore consistent with a coseismic rupture which does not intersect the Enriquillo fault but abuts against the south-dipping Enriquillo fault at shallow depth (2–5 km, Fig. 2, cross-sections A–B and C–D).

Comparison with Previous Slip Models

Our slip inversion is unique in that the fault geometry is predetermined from the detailed aftershock locations of Douilly et al. (2013). As in the studies of Calais et al. (2010) and De Lépinay et al. (2011), we retrieve oblique slip in an
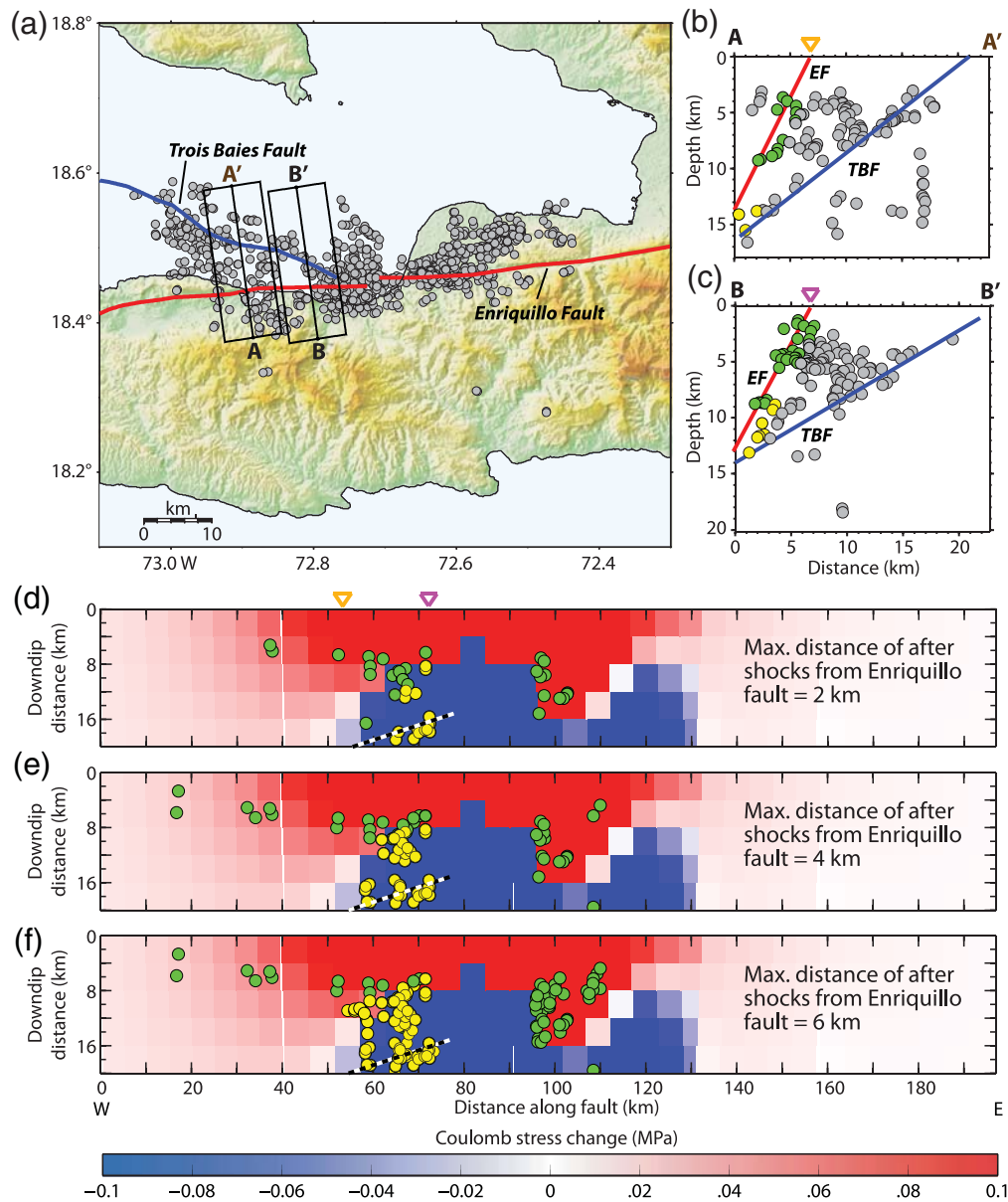
Figure 12. (a) Map view of southern Haiti showing aftershocks associated with the 2010 earthquake and surface fault traces of the Enriquillo and Trois Baies faults. (b–c) Cross sections along lines A–A′ and B–B′ show aftershocks (circles) within the width of the cross-section boxes. Green circles denote aftershocks that are located within 2 km of the Enriquillo fault (EF). Yellow circles denote aftershocks that are located within 2 km of the Enriquillo and Trois Baies (TBF) faults. (d–f) Calculated coseimic Coulomb stress changes resolved on the Enriquillo fault as viewed looking north into the fault. The calculation assumes coseismic slip associated with the optimal coseismic model (Fig. 5c) and a friction coefficient of 0.4. Green circles show aftershocks that are located within 2, 4, and 6 km of the Enriquillo fault in (d), (e), and (f), respectively. Yellow circles show aftershocks that are located within 2, 4, and 6 km of the Enriquillo fault and Trois Baies faults in (d), (e), and (f), respectively. Orange and magenta triangles in (d) show where the surface trace of the Enriquillo fault is located (see b and c). The black dashed line in (d–f) shows where the Trois Baies fault makes contact with the Enriquillo fault based on the assumed geometry of both faults.

eastern patch (segment L2) located at approximately 14 km depth. Although we split the Léogâne fault into two segments with a different orientation for the western segment than these other two models, we also find pure strike-slip motion on the western segment (L1), as in these previous models. Our model is different from Hayes *et al.* (2010) because it consists of two different faults segments, rather

than three, and does not require slip on a vertical segment of the Enriquillo fault. We do not incorporate seismological data, which could account for some of the differences. Also, Douilly *et al.* (2013) demonstrated a systematic bias of the National Earthquake Information Center (NEIC) hypocenters, which only use teleseismic data to the southwest likely due to station coverage, which could explain why Hayes *et al.*
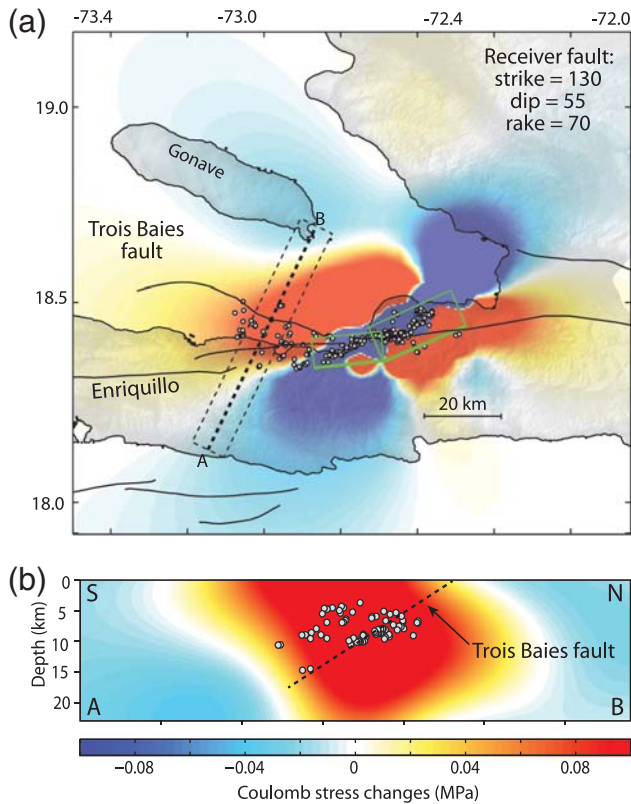
Figure 13. (a) Map view of calculated Coulomb stress change at a depth of 10 km in the Trois Baies fault region along with aftershocks between 8–12 km depth. Receiver faults assume a strike of 130°, a dip of 55° to the south, and a rake of 70° to the south, consistent with the average strike of the surface trace of the Trois Baies fault and the largest aftershocks in this region (Nettles and Hjörleifsdóttir, 2010; Douilly *et al.*, 2013). (b) Cross-sectional view of Coulomb stress changes looking west into line denoted by A–B in (a) along with aftershocks contained in the cross-sectional box. The calculation assumes coseismic slip associated with the optimal coseismic model (Fig. 5c) and a friction coefficient of 0.4. Surface of the best-fit rupture geometry (model A in Fig. 3) is shown with green rectangles.

(2010) proposed a model in which the rupture initiated on the Enriquillo fault. However, the slip pattern on their corresponding Léogâne fault is similar to our findings (i.e., with oblique displacement in its eastern part becoming pure strike slip to the west).

We find approximately the same two slip patches as Meng *et al.* (2012) in spite of their incorrect interpretation of a north-dipping Trois Baies fault, which turns out to have minimal negative impact on their result. This is because their slip is still concentrated in the area we refer to as the central cluster of aftershocks on the Léogâne fault. Our results are consistent with their main conclusion that the rupture continues for a short distance offshore, although we show that it occurs on the continuation of the north-dipping Léogâne fault, and not the south-dipping Trois Baies fault. Hashimoto *et al.* (2011) estimated coseismic slip from an inversion of four interferograms (three of them used in our study). Their slip distribution closely corresponds to the one found here,

with oblique motion in the eastern part of the rupture transitioning to pure strike slip to the west. They argue that the InSAR data requires a shallow Léogâne fault dip (42°), which is not consistent with the relocated aftershock distribution (Douilly *et al.*, 2013).

The 12 January 2010 Haiti earthquake shows striking similarities to the 1989 M_w 6.9 Loma Prieta earthquake that occurred to the southwest of the southern Santa Cruz Mountain segment of the San Andreas fault (e.g., Beroza, 1991). Both were oblique-slip events that occurred on faults in the proximity of, and subparallel to, a major strike-slip fault (the San Andreas fault in the case of the Loma Prieta event). They both involved the rupture of a secondary fault intersecting or abutting the major regional active fault. Both are characterized by two major patches of concentrated slip, and both occurred at depth with no evidence of surface rupture. These analogies perhaps help to understand the hazard that blind oblique thrusts can present under transpressional interseismic strain accumulation. The Haiti event is different from the Loma Prieta event, however, in the spatial extent of aftershocks outside the rupture zone, extending more than 20 km offshore on the Trois Baies fault.

Another similarity between the Loma Prieta event and this earthquake is the fact that the Léogâne rupture appears to abut a section of the major Enriquillo fault, at the central cluster of aftershocks. The source plane of the Loma Prieta is also known to intersect the major San Andreas fault located to the north of the rupture zone. There are other examples of earthquakes on apparently intersecting dipping fault planes, the most notable being the Northridge and San Fernando earthquakes (e.g., Mori *et al.*, 1995; Wald *et al.*, 1996). However, in that case the two faults are conjugate blind thrusts in a compressional environment with shortening nearly perpendicular to the fault trend. The Loma Prieta case presents a challenge similar to the Haiti earthquake in interpreting the intersection of the rupture plane and the vertical San Andreas fault.

Implications for Earthquake Hazard

The 2010 Haiti earthquake helped to relieve the strain accumulated on a 30-km-long span of the transpressional southern Haiti fault zone, which comprises the main Enriquillo and several adjacent active faults. Although GPS measurements do not have the spatial resolution necessary to separate strain accumulation on the Enriquillo versus Léogâne faults, the latter is likely accumulating elastic strain at a slow rate, given the lack of corresponding morphological expression. As a result, one would expect the recurrence time of significant earthquakes on the Léogâne fault to be long. Neighboring faults are more of a concern, in particular the Enriquillo fault, which experienced a calculated increase in Coulomb stress to the west and to the east of the January 2010 rupture.

Active fault segments adjacent to the Léogâne rupture have not produced large earthquakes for at least 250 years

and are thought capable of producing a magnitude *M* 7 or larger earthquake (Manaker *et al.*, 2008). With several highly populated cities located in close proximity, seismic hazard is a concern. New probabilistic seismic-hazard maps have been created for Haiti that better take into account accumulating strain in known fault zones (Frankel *et al.*, 2011). However, these do not take into account time dependent changes in hazard. Therefore, even though the calculated Coulomb stress changes do not provide any indication in the absolute timing of a future event, the study emphasizes the importance of continually improving seismic-hazard estimates in an effort to promote risk reduction in this vulnerable area.

Furthermore, the production of aftershocks on the Trois Baies fault caused by the Léogâne rupture shows that this fault is an active structure, posing an additional threat for the western part of the southern peninsula. The level of activity of the Trois Baies fault is a new concern in terms of seismic hazard for the region, and also raises awareness that this may also be a problem for other poorly-studied offshore thrust faults.

Conclusions

We have updated the geometry and slip distribution of the 12 January 2010 Haiti earthquake using the most precise aftershock locations available to date (Douilly *et al.*, 2013) and a dataset combining GPS, coastal uplift, and InSAR coseismic displacements. Our preferred model involves two main slip patches on adjacent segments of the Léogâne fault, with a combination of reverse and strike-slip motion consistent with several previously published slip inversions. We find that the geodetic and aftershock data do not require slip on faults other than the Léogâne fault, contrary to the more complex model of Hayes *et al.* (2010).

Calculated Coulomb stress changes caused by coseismic slip on the Léogâne fault may explain the aftershock cluster found on the Trois Baies reverse fault as triggered events. The geodetic data does not show evidence for rupture of the Trois Baies fault during the mainshock. We find an increase of calculated Coulomb stress on the Enriquillo fault to the west of the 2010 rupture (Miragoâne area) and to the east near Port-au-Prince, as well as on the near-surface segment adjacent to the 2010 rupture. This indicates that while the 2010 earthquake may have relieved stress on the Léogâne fault, it may have loaded segments of the Enriquillo fault that are already known to be late in their earthquake cycle, potentially advancing the time of occurrence of these hazardous events. Other regional faults do not show a significant increase in static stresses, with the exception of the western edge of the Trois Baies fault and a central segment of the Neiba–Matheux fault (depending on the apparent fault friction assumed).

Coseismic slip during the 12 January 2010 Haiti earthquake released secular strain accumulation over a small fraction of the whole southern peninsula fault zone, which comprises the main Enriquillo fault, as well as secondary compressional faults such as the one responsible for the earth-

quake (Léogâne fault). Increased stresses on the Trois Baies fault (highlighted by aftershock seismicity) and on portions of the Enriquillo fault are a concern as this could advance the timing of future events on these faults. While the Enriquillo fault segments are capable of *M* 7 events given their lengths and the accumulated slip deficit in the area, little is known about the characteristics of offshore faults (such as the Trois Baies fault). This is an important topic for further studies.

These conclusions are based on geological data that are still limited. Our lack of understanding of parameters as fundamental as the dip of the Enriquillo fault along strike, as well as with depth, calls for continued research on the potential seismic sources in southern Haiti and expansion to other thrust faults discussed in this section whose parameters are poorly known. In addition, postseismic stress relaxation will likely alter failure conditions on regional faults, so continued GPS monitoring is particularly important. A reasoned and sustainable reconstruction for Haiti depends on a continued effort to address the remaining uncertainties limiting our understanding of the regional seismic-hazard level.

Data and Resources

Acknowledgments

References

Aki, K. (1979). Characterization of barriers on an earthquake fault, *J. Geophys. Res.* **84,** no. B11, 6140–6148, doi: 10.1029/JB084iB11p06140.

Ali, S. T., A. M. Freed, E. Calais, D. M. Manaker, and W. R. McCann (2008). Coulomb stress evolution in northeastern Caribbean over the past 250 years due to coseismic, postseismic, and interseismic deformation, *Geophys. J. Int.* **174,** 904–918.

Bakun, W. H., C. H. Flores, and U. S. ten Brink (2011). Significant earthquakes on the Enriquillo fault system, Hispaniola, 1500–2010: Implications for seismic hazard, *Bull. Seismol. Soc. Am.* **102,** no. 1, 18–30, doi: 10.1785/0120110077.

Barnhart, W. D., and R. B. Lohman (2010). Automated fault model discretization for inversions for coseismic slip distributions, *J. Geophys. Res.* **115,** no. B10419, doi: 10.1029/2010JB007545.

Bellerive, J. M. (2010). Haiti: PDNA du tremblement de terre—évaluations des dommages, des pertes et des besoins généraux et sectoriels, http://www.gfdrr.org/sites/gfdrr.org/files/documents/GFDRR_Haiti_PDNA_2010_FR.pdf, last accessed April 2013.

Benford, B., C. DeMets, and E. Calais (2012). GPS estimates of microplate motions, northern Caribbean: Evidence for a Hispaniola microplate and implications for earthquake hazard, *Geophys. J. Int.* **191,** 481–490, doi: 10.1111/j.1365-246X.2012.05662.x.

Beroza, G. C. (1991). Near source modeling of the Loma Prieta earthquake: Evidence for heterogeneous slip and implications for earthquake hazard, *Bull. Seismol. Soc. Am.* **81,** 1603–1621.

Beroza, G. C., and P. Spudich (1988). Linearized inversion for fault rupture behavior: Application to the 1984 Morgan Hill, California earthquake, *J. Geophys. Res.* **93,** no. B6, 6275–6296, doi: 10.1029/JB093iB06p06275.

Calais, E., A. M. Freed, G. Mattioli, F. Amelung, S. Jonsson, P. Jansma, S. H. Hong, T. Dixon, C. Prepetit, and R. Momplaisir (2010). Transpressional rupture of an unmapped fault during the 2010 Haiti earthquake, *Nat. Geosci.* **3,** doi: 10.1038/ngeo992.

Cormier, M., C. M. McHugh, S. P. Gulick, N. Braudy, M. B. Davis, J. B. Diebold, N. Dieudonne, R. Douilly, M. J. Hornbach, H. J. Johnson, K. Mishkin, L. Seeber, C. C. Sorlien, M. J. Steckler, S. J. Symithe, and J. Templeton (2010). Vertical deformation of late quaternary features across Port-au-Prince Bay, Haiti, Presented at *2010 Fall Meeting AGU*, San Francisco, California, 13–17 December, Abstract U13A–0005.

De Lépinay, B., A. Deschamp, F. Klingelhoefer, Y. Mazabraud, B. Delouis, V. Clouard, Y. Hello, J. Crozon, B. Marcaillou, D. Graindorge, M. Vallée, J. Perrot, M.-P. Bouin, J.-M. Saurel, P. Charvis, and M. St-Louis (2011). The 2010 Haiti earthquake: A complex fault pattern constrained by seismologic and tectonic observations, *Geophys. Res. Lett.* **38,** L22305, doi: 10.1029/2011GL049799.

Delouis, B., M. Vallée, M. Meghraoui, E. Calais, S. Maouche, K. Lammali, A. Mahsas, P. Briole, F. Benhamouda, and K. Yelles (2004). Slip distribution of the 2003 Boumerdes–Zemmouri earthquake, Algeria, from teleseismic, GPS, and coastal uplift data, *Geophys. Res. Lett.* **31,** L18607, doi: 10.1029/2004GL020687.

Doser, D. I., and H. Kanamori (1986). Depth of seismicity in the Imperial Valley region (1977–1983) and its relationship to heat flow, crustal structure, and the October 15 1979 earthquake, *J. Geophys. Res.* **91,** 675–688.

Douilly, R., J. S. Haase, W. L. Ellsworth, M. P. Bouin, E. Calais, S. J. Symithe, J. G. Armbruster, B. de Lepinay, A. Deschamps, S. L. Mildor, M. Meremonte, and S. E. Hough (2013). Crustal structure and fault geometry of the 2010 Haiti earthquake from temporary 643 seismometer deployments, *Bull. Seismol. Soc. Am.* **103,** no. 4, doi: 10.1785/0120120303.

Felzer, K. R., T. W. Becker, R. E. Abercrombie, G. Ekström, and J. R. Rice (2002). Triggering of the 1999 M_w 7.1 Hector Mine earthquake by aftershocks of the 1992 M_w 7.3 Landers earthquake, *J. Geophys. Res.* **107,** no. B9, 2190.

Frankel, A., S. Harmsen, C. Mueller, E. Calais, and J. Haase (2011). Seismic hazard maps For Haiti, *Earthq. Spectra* **27,** S23–S41, doi: 10.1193/1.3631016.

Freed, A. (2005). Earthquake triggering by static, dynamic, and postseismic stress transfer, *Annu. Rev. Earth Planet. Sci.* **33,** doi: 10.1146/annurev.earth.33.092203.122505.

Hardebeck, J. L., J. J. Nazareth, and E. Hauksson (1998). The static stress change triggering model: Constraints from two southern California aftershock sequences, *J. Geophys. Res.* **103,** no. B10, 24427–24437, doi: 10.1029/98JB00573.

Harris, R. A., and P. Segall (1987). Detection of a locked zone at depth on the Parkfield, California segment of the San Andreas fault, *J. Geophys. Res.* **92,** no. B8, 7945–7962.

Harris, R. A., and R. W. Simpson (1992). Changes in static stress on southern California faults after the 1992 Landers earthquake, *Nature* **380,** 251–254.

Hartzell, S. H., and T. H. Heaton (1986). Rupture history of the 1984 Morgan Hill, California earthquake from the inversion of strong motion records, *Bull. Seismol. Soc. Am.* **76,** 649–674.

Hashimoto, M., Y. Fukushima, and Y. Fukahata (2011). Fan-delta uplift and mountain subsidence during the Haiti 2010 earthquake, *Nat. Geosci.* **4,** 255–259.

Hayes, G. P., R. W. Briggs, A. Sladen, E. J. Fielding, C. Prentice, K. Hudnut, P. Mann, F. W. Taylor, A. J. Crone, R. Gold, T. Ito, and M. Simons (2010). Complex rupture during the 12 January 2010 Haiti earthquake, *Nat. Geosci.* **3,** 800–805, doi: 10.1038/ngeo977.

Helmstetter, A., Y. Y. Kagan, and D. D. Jackson (2005). Importance of small earthquakes for stress transfers and earthquake triggering, *J. Geophys. Res.* **110,** no. B5, B05S08.

Houston, H., and E. R. Engdahl (1989). A comparison of the spatio-temporal distribution of moment release for the 1986 Andreanof Islands earthquake with relocated seismicity, *Geophys. Res. Lett.* **16,** no. 12, 1421–1424, doi: 10.1029/GL016i012p01421.

Jonsson, S., H. Zebker, and P. Segall (2002). Fault slip distribution of the M_w 7.2 Hector Mine earthquake estimated from satellite radar and GPS measurements, *Bull. Seismol. Soc. Am.* **92,** 1377–1389.

King, G. C. P., and M. Cocco (2001). Fault interaction by elastic stress changes: New clues from earthquake sequences, *Adv. Geophys.* **44,** 1–38.

King, G. C. P., R. Stein, and J. Lin (1994). Static stress changes and the triggering of earthquakes, *Bull. Seismol. Soc. Am.* **84,** 935–953.

Lawson, C. L., and R. J. Hanson (1974). *Solving Least Squares Problems*, Prentice-Hall, Englewood Cliffs, New Jersey, 337 pp.

Lin, J., and R. S. Stein (2004). Stress triggering in thrust and subduction earthquakes and stress interaction between the southern San Andreas and nearby thrust and strike-slip faults, *J. Geophys. Res.* **109,** no. B02303, doi: 10.1029/2003JB002607.

Lin, J., R. S. Stein, V. Sevilgen, and S. Toda (2010). Coulomb Stress Transfer Model for the January 12 2010 M_w 7.0 Haiti earthquake, *U.S. Geol. Surv. Open-File Rept. 2010-1019.*

Manaker, D. M., E. Calais, A. M. Freed, S. T. Ali, P. Przybylski, G. Mattioli, P. Jansma, C. Prépetit, and J. B. de Chabalier (2008). Interseismic plate coupling and strain partitioning in the northeastern Caribbean, *Geophys. J. Int.* **174,** 889–903.

Mann, P., F. Taylor, R. Edwards, and T. Ku (1995). Actively evolving microplate formation by oblique collision and sideways motion along strike-slip faults: An example from the northeastern Caribbean plate margin, *Tectonophysics* **246,** 1–69.

McHugh, C. M., L. Seeber, N. Braudy, M. H. Cormier, M. B. Davis, J. B. Diebold, N. Dieudonne, R. Douilly, S. P. Gulick, M. J. Hornbach, H. E. Johnson, K. R. Mishkin, C. C. Sorlien, M. J. Steckler, S. J. Symithe, and J. Templeton (2011). Offshore sedimentary effects of the 12 January 2010 Haiti earthquake, *Geology* **39,** 723–726, doi: 10.1130/G31815.1.

Mendoza, C., and S. H. Hartzell (1988). Aftershock patterns and main shock faulting, *Bull. Seismol. Soc. Am.* **78,** 1438–1449.

Meng, L., J. P. Ampuero, A. Sladen, and H. Rendon (2012). High-resolution backprojection at regional distance: Application to the Haiti M 7.0 earthquake and comparisons with finite source studies, *J. Geophys. Res.* **117,** doi: 10.1029/2011JB008702.

Momplaisir, R. (1986). Contribution à l'Etude Géologique de la partie orientale du massif de la Hotte (Presqu'Ile du Sud d'Haiti): Synthèse structurale des marges de la presqu'ile à partir de données sismiques, *Ph.D. Thesis*, University of Paris, Paris, France.

Mori, J., D. J. Wald, and R. L. Wesson (1995). Overlapping fault planes of the 1971 San Fernando and 1994 Northridge, California earthquakes, *Geophys. Res. Lett.* **22,** 1033–1036, doi: 10.1029/95GL00712.

Nettles, M., and V. Hjörleifsdóttir (2010). Earthquake source parameters for the 2010 January Haiti main shock and aftershock sequence, *Geophys. J. Int.* **183,** 375–380, doi: 10.1111/j.1365-246X.2010.04732.x.

Okada, Y. (1992). Internal deformation due to shear and tensile faults in a half-space, *Bull. Seismol. Soc. Am.* **82,** 1018–1040.

Page, M. T., S. Custdio, R. J. Archuleta, and J. M. Carlson (2009). Constraining earthquake source inversions with GPS data: 1. Resolution-based removal of artifacts, *J. Geophys. Res.* **114,** no. B01314, doi: 10.1029/2007JB005449.

Parsons, T., R. S. Stein, R. W. Simpson, and P. A. Reasenberg (1999). Stress sensitivity of fault seismicity: A comparison between limited-offset oblique and major strike-slip faults, *J. Geophys. Res.* **104,** 20183–20202.

Prentice, P. S., P. Mann, A. J. Crone, R. D. Gold, K. W. Hudnut, R. W. Briggs, R. D. Koehler, and P. Jean (2010). Seismic hazard of the Enriquillo–Plantain Garden fault in Haiti inferred from palaeoseismology, *Nat. Geosci.* **3,** 789–793, doi: 10.1038/ngeo991.

Pubellier, M., A. Mauffret, S. Leroy, J. Vila, and H. Amilcar (2000). Plate boundary readjustment in oblique convergence: Example of the Neogene of Hispaniola, Greater Antilles, *Tectonics* **19,** 630–648.

Reasenberg, P. A., and R. W. Simpson (1992). Response of regional seismicity to the static stress change produced by the loma prieta earthquake, *Science* **255,** 1687–1690.

Rybicki, K. (1973). Analysis of aftershocks on the basis of dislocation theory, *Phys. Earth. Planet. Int.* **7,** 409–422.

Scherer, J. (1912). Great earthquakes in the island of Haiti, *Bull. Seismol. Soc. Am.* **2,** 161–180.

Simons, F. J., R. D. Van Der Hilst, J. P. Montagner, and A. Zielhuis (2002). Multimode Rayleigh wave inversion for heterogeneity and azimuthal anisotropy of the Australian upper mantle, *Geophys. J. Int.* **151,** 738–754, doi: 10.1046/j.1365-246X.2002.01787.x.

Steacy, S., J. Gomberg, and M. Cocco (2005). Introduction to special section: Stress transfer, earthquake triggering, and time-dependent seismic hazard, *J. Geophys. Res.* **110,** no. B05S01, doi: 10.1029/2005JB003692.

Stein, R. S., A. A. Barka, and J. H. Dieterich (1997). Progressive failure on the northern Anatolian fault since 1939 by earthquake stress triggering, *Geophys. J. Int.* **128,** 594–604.

Sudhaus, H., and S. Jonsson (2009). Improved source modeling through combined use of InSAR and GPS under consideration of correlated data errors: Application to the June 2000 Kleifarvatn earthquake, Iceland, *Geophys. J. Int.* **176,** 389–404.

Toda, S., and R. S. Stein (2002). Response of the San Andreas fault to the 1983 Coalinga–Nunez earthquakes: An application of interaction-based probabilities for Parkfield, *J. Geophys. Res.* **107,** no. B6, 2126, doi: 10.1029/2001JB000172.

Wald, D. J., T. H. Heaton, and K. W. Hudnut (1996). The slip history of the 1994 Northridge, California earthquake determined from strong motion, teleseismic, GPS, and leveling data, *Bull. Seismol. Soc. Am.* **86,** S49–S70.

Waldhauser, F. (2001). hypoDD—A Program to Compute Double-Difference Hypocenter Locations (hypoDD version 1.0-03/2001), *U.S. Geol. Surv. Open-File Rept. 01-113.*

Welstead, S. T. (1999). *Fractal and wavelet image compression techniques,* SPIE Optical Engineering Press, Bellingham, Washington, 232 pp.

Wessel, P., and W. H. F. Smith (1998). New, improved version of the generic mapping tools released, *EOS Trans. AGU* **79,** 579, doi: 10.1029/98EO00426.

Zoback, M. D., M. L. Zoback, V. S. Mount, J. Suppe, J. P. Eaton, J. H. Healy, D. Oppenheimer, P. Reasenberg, L. Jones, C. B. Raleigh, I. G. Wong, O. Scotti, and C. Wentworth (1987). New evidence on the state of stress of the San Andreas fault system, *Science* **238,** 1105–1111.

Department of Earth and Atmospheric Sciences
Purdue University
West Lafayette, Indiana 47907
   (S.J.S., A.M.F., R.D.)

Ecole Normale Supérieure
Department of Geosciences
UMR CNRS 8538
75231 Paris cedex 5, France
   (E.C.)

Scripps Institution of Oceanography
University of California, San Diego
La Jolla, California 92093-0225
   (J.S.H.)